ACS MATERIALS LETTERS

Cite This: ACS Materials Lett. 2019, 1, 71−76

www.acsmaterialslett.org

LETTER

Mapping Charge Percolation in Flowable Electrodes Used in Capacitive Deionization

Marm B. Dixit,[†] Daniel Moreno,[‡] Xianghui Xiao,[¶] Marta C. Hatzell,*[,‡] and Kelsey B. Hatzell*[,†]

[†]Department of Mechanical Engineering, Vanderbilt University, Nashville, Tennessee 37203, United States

[‡]George W. Woodruff School of Mechanical Engineering, Georgia Institute of Technology, Atlanta, Georgia 30313, United States

[¶]National Synchrotron Light Source II, Brookhaven National Laboratory, Upton, New York 11973, United States

Supporting Information

ABSTRACT: Electrical percolation in flow electrode capacitive deionization is critical to mitigate electronic resistance and maximize ion electrosorption. It is experimentally challenging to characterize mass and charge transfer phenomena in flow electrodes with space and time dimensions. Here, we demonstrate a way to resolve charge percolation pathways at sub-micron resolutions using synchrotron X-ray tomography and computational techniques. Three-dimensional reconstructed images provide a means to measure important micro- and mesoscale electrode properties, such as pore-size distribution, aggregation size, and percolation properties. Developing this microstructural understanding of flow-electrodes is necessary to understand how transport limitations impact separations performance and to inform operating conditions at the technology level (flow regimes).

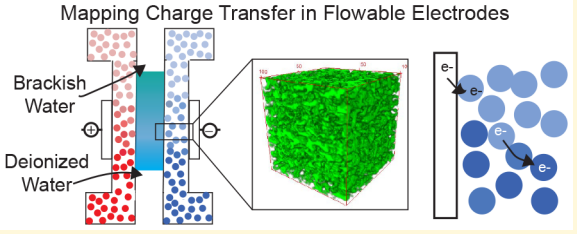

Integrating renewable energy with desalination technologies is an important challenge for the design of resilient and decoupled water and energy infrastructures. One integrated technology capable of directly using renewable electrons for salt-based separations is capacitive deionization (CDI).[1−3] CDI performs ion removal using an electrosorption-based process. Separation is achieved through storing ions within an electric double layer on a high surface area carbon-based electrode. Thus, salt removal is limited by the effective surface area of the electrode which results in the need for batch-mode operation. In a batch operational mode, ion removal occurs during a charging period. After the active material's surface area is completely saturated with ions, the process is reversed. During this reversal, a negative or zero voltage is applied to the CDI cell to create a high concentration waste brine. This intermittent batch operation has relegated CDI to the treatment of low salinity feeds with low volume requirements.[4]

An alternative approach to conventional CDI is flow-electrode capacitive deionization (FCDI).[5−7] Instead of utilizing stationary electrodes, flow-electrodes suspend the active material in a solution and flow the active material in parallel to the feed water stream (Figure 1a). Flowable electrodes are composed of active materials (activated carbon) at loading's between 5−20 wt % and an ionic electrolyte. There are fundamental trade-offs between active material loading and flowability. This advancement enables treatment of higher concentration solutions (>35 g/L), longer salt removal times, and continuous operation. Nevertheless, semi-solid flowable electrodes are currently plagued by low energy recovery and high resistance. High loading leads to a potential for high salt removal but at the expense of pumping power. Within the flowable electrode, there are two fundamental processes that govern performance: (1) charge transfer (Figure 1b) and (2) ionic adsorption. These two processes are coupled and ion adsorption (salt removal) is thus limited to material or particles that can maintain charge during flow operation. Note that electrodialytic processes can aid ionic transport but are marginalized with elevated carbon loading.[8]

The three main limitations for FCDI are (1) charge leakage, (2) high electrical resistance, and (3) energetic losses induced by pumping (hydrodynamics effects). All three of these issues exist because of the intermittent interactions between the active materials within a flow electrode (particle−particle interactions). Currently, there is a deficit of visualization and in situ experimentation techniques that are capable of probing these local interactions. This is in part because flowable electrodes are 3-D, biphasic, and opaque. To overcome this challenge, recently, it was demonstrated that 3-D synchrotron radiation X-ray tomography and optical imaging techniques could be used to observe particle interactions at various length scales.[9,10] Understanding micron-level mechanisms and transport processes is important for engineering biphasic flowable electrodes for energy efficient ion removal. Furthermore, insight at this scale can be instrumental for deriving control

Received: April 10, 2019
Accepted: May 15, 2019
Published: May 15, 2019

DOI: 10.1021/acsmaterialslett.9b00106
ACS Materials Lett. 2019, 1, 71−76

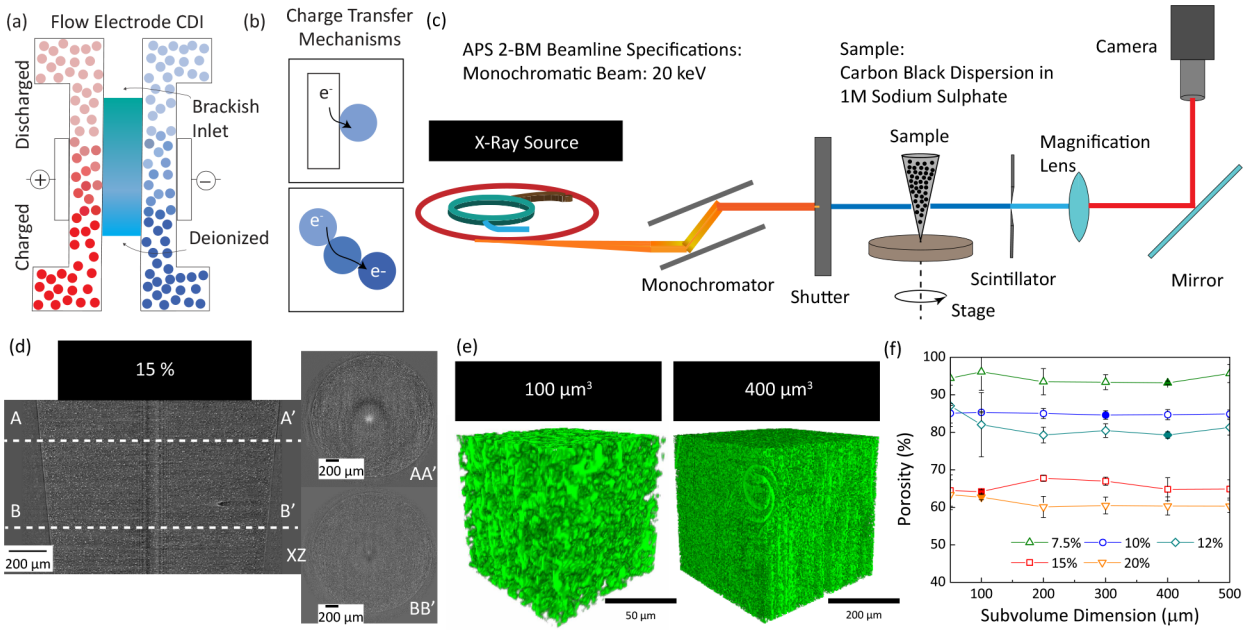

Figure 1. Flow electrode capacitive deionization uses a scalable architecture for continuous desalination (a). Separation is only achieved if charge transfer can occur throughout the thick, biphasic, flow-electrode. Charge transfer can occur through the current collector and through particle−particle contact (b). Synchrotron radiation X-ray tomographic microscopy can discern between different phases (solid and liquid), when probed with high-energy X-rays (c). A radiographic image demonstrates contrast between carbon and water (d). These radiographic images can be reconstructed into 3-dimensional images (e). Large-volume reconstructions are computationally intense. Subvolume analysis allows for optimizing reconstruction field of view without sacrificing relevant microstructure detail (f).

strategies for macroscopic operational parameters, improving cell design, and can be used for improved multi-scale models of flowable electrode systems. Beyond flowable electrode systems, understanding ionic transport in percolated packed beds is broadly important for various adsorption-based processes. Herein, we aim to evaluate fundamental transport properties in flowable electrodes using synchrotron X-ray tomography and correlate these properties to electrochemical deionization performance through benchtop experimentation (Figure 1c). Furthermore, the resilience of the visualization technique is systematically evaluated for different subvolumes between 100 and 500 μm^3 and reconstructed microstructures are evaluated for charge transport pathways.

In this work, activated carbon (YP-50, Kuraray Co. Ltd) and salts (sodium sulfate and sodium chloride, Fisher Scientific) were used for all experiments. Flowable electrodes were prepared with varying carbon loadings between 5 and 20 wt %. Components were mixed with a magnetic stirring over low heat. The heat increases the wettability of the carbon. Carbon was added directly to a salt solution (Na_2SO_4/NaCl) depending on the experiment (imaging/desalination). Flowable electrodes are colloidally stable when a small amount of salt is added, and sedimentation was not observed over the duration of desalination or imaging tests.

Synchrotron X-ray tomography studies were carried out at the 2-BM beamline of the Advanced Photon Source (Figure 1c). The incident X-rays were filtered with a monochromator to a single energy of 20 keV. Projections (1500) were taken evenly during a 180° sample rotation with 30 ms exposure time for each projection. A Mitutoyo long-working distance 10× magnification lens was used with a pco.edge5.5 camera. The resultant voxel size was 0.65 μm and a field of view of 1.4 × 0.8 mm^2. The raw tomography data was reconstructed using Tomopy software.[11]

Synchrotron X-ray tomographic microscopy enables direct visualization of flow electrode microstructural features. Unlike indirect techniques (i.e. rheology and electrochemistry), X-rays are capable of distinguishing between different materials and phases with varying absorption properties (Figure 1c). The mass absorption coefficient for carbon and water at 20 keV is ∼0.43 and ∼0.79, respectively.[12] During imaging experiments the X-ray source and detector are typically stationary and the sample rotates. Liquids and colloidal systems are challenging to image because movement of the liquid or solid phase can lead to blurry images. Flowable electrodes with even a small amount of salt (100 mM) are stable, and thus, all samples described, herein, were imaged in 1 M sodium sulfate. Furthermore, to minimize liquid movement, samples were mounted in line with the X-ray source in a sealed pipette (Figure 1c). Carbon and water are distinguishable in radiographic projections when probed with a monochromatic beam at 20 keV (Figure 1d). Raw images are segmented based on an appropriate threshold grayscale value to yield sets of binarized images depicting the carbon and the solution phase. A typical tomographic scan captures a large field of view (∼4 × 0.8 mm^2). Carrying out image analysis on the entire field of view of the flowable electrode is computationally intense; therefore, geometric analysis was completed on varying subvolumes between 100 and 500 μm^3 to probe microstructure sensitivity (Figure 1e and f).

Microstructure-derived material properties obtained from segmented data are sensitive to the image processing protocols, the binarization algorithms, and the domain sizes.[13] Flow electrode porosity was evaluated over a range of subvolume sizes to identify the representative subvolume for property characterization. Samples with lower solid loading show an optimal subvolume size of 300-400 μm^3, while at higher loading, 100 μm^3 is the optimal subvolume (Figure 1f). Smaller

DOI: 10.1021/acsmaterialslett.9b00106
ACS Materials Lett. 2019, 1, 71−76

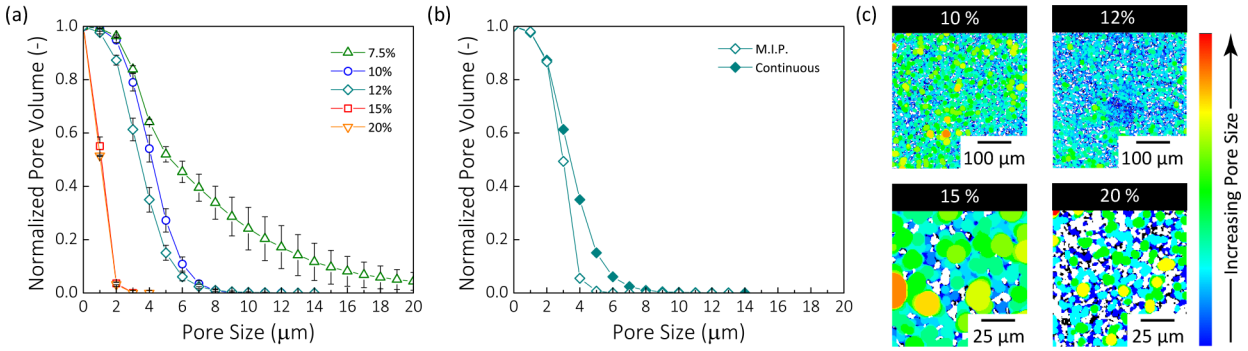

Figure 2. Pore size distributions for flow electrode computed from the tomography data (a). Comparison of pore size distribution obtained from continuous and mercury intrusion porosimetry (MIP) algorithms (b). Pore size maps for 2D slices (c).

subvolumes do not capture the effective microstructure at low solid loading and hence lead to higher deviation in these cases. Artifacts like bubble formation, sedimentation, and particle or fluid movement during scans can lead to higher microstructure heterogeneity for larger subvolumes at higher solid loading. In a flowable electrode, the solution phase provides ionic transport pathways, and the carbon region influences electron transport and ion storage properties. The carbon has several length scales which impact flow electrode performance. At the nanoscale, incomplete carbon wetting can decrease the accessible surface area and ion removal capacity. At the micro- and mesoscale, electrical percolation between aggregated active materials plays a significant role on material utilization. Synchrotron X-ray tomography enables quantification of micro- and mesoscale structural properties. Important mesoscale properties include pore size distribution, aggregation size, and percolation properties.

The two boundaries for flow-electrode microstructure descriptors are (1) perfectly disperse active material, where aggregation is minimized, or (2) highly aggregated and phase separated structures. In reality, the structure of a flowable electrode falls between these two boundaries and is transient depending on the operating conditions (plug flow or continuous). A common microstructure-descriptor for solid or dry materials is a pore size distribution. The pore size traditionally refers to a non-solid region or gas phase in a material. This concept can be translated to flow-electrode microstructures in discerning microstructure properties for the solution phase. Pore size or solution size distributions is carried out by fitting spheres of different radii in the solution space of the binarized stack. The histogram of the sphere radii represents the size distribution of a phase inside the sample. For this study, the solution space in the flow electrode is identified as the porous region and the interstitial space between the particles is described as the pore size distribution. The porosity of the samples measured from tomography reconstructions correlate well to the solid loading of the flow electrodes. The maximum pore size drops from ≥20 μm for 5 wt % system to ∼2 μm for the 15 and 20 wt % system (Figure 2a and c). Activated carbon has a lower density (∼0.2−0.3 g cm^{-3}) compared to water (1 g cm^{-3}) that results in increased volume fraction at higher solid loading. Activated carbon occupies ∼50% of the volume at 20 wt % solid loading. Thus, the interstitial space between particles drops significantly with increase in the solid loading. A smaller, less contiguous solution phase is expected in the higher loading systems. The pore size distributions were evaluated with two different algorithms to assess the sensitivity of pore size quantification (Figure 2b). The "continuous PSD" method and "mercury intrusion porosimetry" (MIP) method use a similar approach, but the spheres are intruded into the stack volume from a specified face for MIP method while are randomly placed for continuous PSD method. The former is done to simulate the conditions that occur in a typical mercury intrusion experiment. Results from both simulation techniques yielded similar pore size distributions indicating a robust quantitative data set (Figure 2b). The differences in pore sizes can also be visualized qualitatively in the pore size maps plotted for representative 2D sections of the flow electrodes (Figure 2c). It should be noted that the representative volumes for 10 and 12 wt % system is 400 μm, while it is 100 μm for 15 and 20 wt % system. The pore sizes decrease from 10 to 12 wt % and from 15 to 20 wt % system. The images also show the increasing particle network sizes represented as the white regions in the figures.

Electron transport in flowable electrodes only occurs at current collectorlactive material interfaces and active materiall active material interfaces. The latter can emerge because of aggregation properties or contact interactions during flow operation. Mapping electrical conduction pathways is critical to understand material utilization and loss mechanisms. In traditional capacitive deionization systems, the active material takes the form of a thin film because it is well documented that material utilization decreases with electrode thickness due to mass transport limitations.[14,15] In contrast, flowable electrodes have unique microstructures and are thick (≥0.5 mm). Mapping electrical percolation in these structures from X-ray reconstructions is challenging because it requires complex meshing of the solid regions. Furthermore, because of the resolution of the technique (∼0.65 μm), there is some sensitivity in the reconstruction. Thus, the inverse approach of mapping ion transport pathways through the solution phase is an indirect way of mapping electron transport. Assuming the electrical percolation only occurs through the solid region and ion transport exclusively through the solution phase, we can correlate regions with high ion flux as regions with low electron conduction. This is a reasonable assumption because carbon will not conduct ions in its bulk.

Ion flux simulations were carried out in the solution phase in order to quantify tortuosity in the *XX*, *YY*, and *ZZ* directions. Transport in these systems is governed by several driving forces, such as advective transport arising from pressure driven flow, mass transport due to concentration gradients, and mass transport due to electric potential gradients. In our analysis, we

DOI: 10.1021/acsmaterialslett.9b00106
ACS Materials Lett. 2019, 1, 71−76

considered only concentration gradients, and the particles are assumed to be stationary in the simulation domain to simplify the simulation process. Since tortuosity is a geometric property dependent on the microstructure of the domain, the former assumption can be safely made. Stationary particles is a potentially limiting assumption as shear forces can significantly alter the microstructure during flow. However, it can be used as a first estimate to understand the effect of solid microstructure on the flux through the water phase. Simulations show flux density through the domain projected on a single plane (Figure 3). The brighter areas (yellow) in the

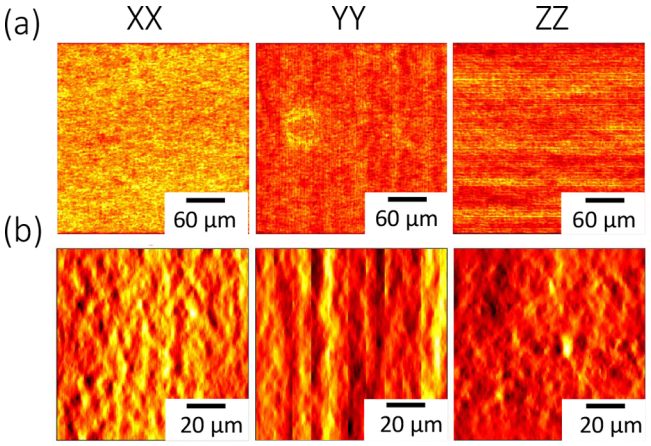

Figure 3. Ion flux distribution through the water phase for 10% (a) and 20 % (b) suspensions across three principle axes.

images represent regions of higher flux (low electron conduction), while darker regions (black) show regions of low ion flux (high electron conduction).[16] Flux projections along the three principle axis at 10% solid loading show very uniform distributions (Figure 3a). The tortuosity values along the three axes are 1.14 ± 0.01, 1.14 ± 0.02, and 1.24 ± 0.02 (*XX*, *YY*, and *ZZ* axes). This suggests that the particle network is discrete and does not significantly increase the transport pathway across the domain. Discrete structure signifies limited electron conduction pathways. The connected particulate network increases with increased solid loading (Figure 3a). This leads to an increasingly tortuous path for ion to transport through the water phase. This is clearly observed in the flux projections for 20 wt % system (Figure 3b). The tortuosity values along the three axes for this system are 1.45 ± 0.02, 1.55 ± 0.09, and 2.35 ± 0.12. The system shows a higher tortuosity, as well as directional anisotropy, suggesting a random particle network in the domain. Directional anisotropy in terms of ion flux may also lead to directional anisotropy in regards to electron conduction mechanisms. Thus, while high solid content loaded flowable electrodes have a higher specific surface area, the charging process may be spatially nonuniform.

Additional information about the packing of the solid particles is obtained by evaluating their geometric tortuosity. Skeletonization of the binarized data set is carried out to yield a 3D skeleton. A skeleton is generated by plotting a line equidistant from boundaries of a domain throughout the domain to yield information about the topology, connectivity, length and direction.[17,18] The geometric tortuosity is estimated by the ratio of actual length to the Euclidean length of the segments of the skeleton map. The geometric tortuosity of the carbon phase increases from 1.2 to 1.55 as the solid loading increases from 5 to 20 wt % (Figure 4a). Correspondingly, the porosity decreases from 93.15 to 62%. Porosity in these systems represent the water phase in the flow electrodes. The higher geometric tortuosity indicates a longer mean free path for ion transport in the carbon phase, which can improve the overall charge transfer properties of the system.

Building effective structure-property relationships for flowable electrodes may provide a way to tailor flow conditions (rheology) and operating modes (plug-flow) for tailored performances (ion removal capacity or rate)[19,20] (Figure S1). Desalination properties carried out in batch mode in this study indicated a clear improvement in the overall salt removal with increased carbon loadings of up to 15 wt%. Salt concentration in the feed was reduced from approximately 90% to around 70% by increasing the loadings from 5 to 15 wt% (Figure 4b). The reported values for salt removal were 91% ± 1% for the 5 wt% loading, 81% ± 3% for the 10 wt% loading, and 69% ± 3% for the 15 wt% loading. This forms a linear trend with R^2 = 0.9994. The average salt removal rate during both the charging and discharging stages of the cycle, not adjusted for electrode mass, also followed a linear trend: 0.87 ± 0.29, 2.94 ± 0.81, and 4.89 ± 0.94 mg/min, for 5%, 10%, and 15% weight loadings (R^2 = 0.9997). However, when measured relative to the carbon loading used, the increases in salt adsorption capacity and average salt adsorption rate is not proportional to the carbon content in the flow electrode.

At higher carbon content loading, electrodes are strongly percolated, but display anisotropy in electron conduction pathways. This anisotropy may contribute to the nonlinear relationship between carbon content and the average salt adsorption rate and salt adsorption capacity (Figure 4c). For example, the salt adsorption capacity (SAC) was 2 ± 0.5 (5 wt

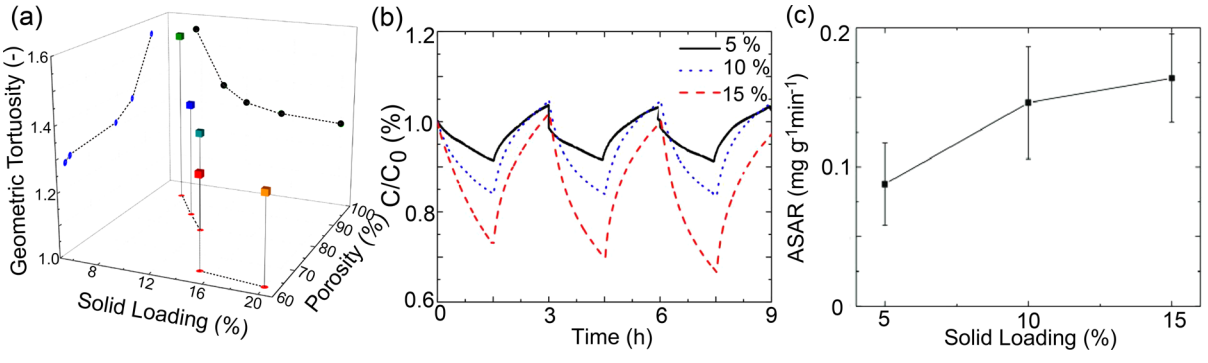

Figure 4. Geometric tortuosity and porosity for flow electrodes (a), desalination tests (b), and average salt adsorption rate (c).

DOI: 10.1021/acsmaterialslett.9b00106
ACS Materials Lett. 2019, 1, 71−76

%), 2.7 ± 0.4 (10 wt%), and 2.9 ± 0.3 mg/g (15 wt%). Additionally, average salt adsorption rate (ASAR) values increased with carbon content 0.09 ± 0.03 (5 wt%), 0.14 ± 0.04 (10 wt%), and 0.16 ± 0.03 mg/g/min (15 wt%) (Figure 4c). Thus, while high carbon loading is anticipated to provide gains because of the greater electrical conduction and larger surface area, the full performance benefit is not fully observed. The origin of this limitation may occur because of anisotropic charging mechanisms.

Understanding the structure of porous materials used for adsorbents is historically a critical step needed to assess various kinetic and transport related properties.[21] With the development of flow-electrode-based electrosorbents there are several challenges in capturing key properties, such as degree of percolation and voids between particles. Without this knowledge, a complete understanding regarding the separations performance cannot be discerned. Here, we explore the use of X-ray tomography as a means to map fundamental properties related to percolation within flow electrodes for capacitive deionization. This information can then be used directly in theoretical models to predict ionic and electronic transport within the flow electrode and to predict the degree of material utilization under various conditions (flow, ionic strength, material weight percentage). Future experiments under flow may provide insight into structural transformations that occur during realistic operational modes. Since electrode structure impacts electron transport mechanisms, this is important for improving separation efficiencies via engineering controlled operating modes (i.e. intermittent plug-flow vs continuous operation).

■ ASSOCIATED CONTENT

Supporting Information

The Supporting Information is available free of charge on the ACS Publications website at DOI: 10.1021/acsmaterialslett.9b00106.

Flow electrode capacitive deionization experimental details and tomography data analysis (PDF)

■ AUTHOR INFORMATION

Corresponding Authors

*E-mail: marta.hatzell@me.gatech.edu.

*E-mail: kelsey.b.hatzell@vanderbilt.edu. Phone: +1 404-385-4503.

ORCID

Marta C. Hatzell: 0000-0002-5144-4969

Kelsey B. Hatzell: 0000-0002-5222-7288

Notes

The authors declare no competing financial interest.

■ ACKNOWLEDGMENTS

This material is based upon work supported by the National Science Foundation under Grant No. 1706290 for M.C.H. and Grant No. 1706956 for K.B.H. The authors acknowledge the Vanderbilt Institute of Nanoscience and Engineering (VINSE) for access to their shared characterization facilities. This research used resources of the Advanced Photon Source, a U.S. Department of Energy (DOE) Office of Science User Facility operated for the DOE Office of Science by Argonne National Laboratory under Contract No. DE-AC02-06CH11357. This research used resources of the National Synchrotron Light Source II, a U.S. Department of Energy (DOE) Office of Science User Facility operated for the DOE Office of Science by Brookhaven National Laboratory under Contract No. DE-SC0012704.

■ REFERENCES

(1) Porada, S.; Zhao, R.; Van Der Wal, A.; Presser, V.; Biesheuvel, P. Review on the science and technology of water desalination by capacitive deionization. *Prog. Mater. Sci.* **2013**, *58*, 1388−1442.

(2) Biesheuvel, P. et al. Capacitive Deionization—Defining a Class of Desalination Technologies. 2017, arXiv:1709.05925. arXiv.org e-Print archive. https://arxiv.org/abs/1709.05925.

(3) Biesheuvel, P.; Van der Wal, A. Membrane capacitive deionization. *J. Membr. Sci.* **2010**, *346*, 256−262.

(4) Zhang, J.; Hatzell, K. B.; Hatzell, M. C. A combined heat-and power-driven membrane capacitive deionization system. *Environ. Sci. Technol. Lett.* **2017**, *4*, 470−474.

(5) Hatzell, K. B.; Hatzell, M. C.; Cook, K. M.; Boota, M.; Housel, G. M.; McBride, A.; Kumbur, E. C.; Gogotsi, Y. Effect of oxidation of carbon material on suspension electrodes for flow electrode capacitive deionization. *Environ. Sci. Technol.* **2015**, *49*, 3040−3047.

(6) Hatzell, K. B.; Iwama, E.; Ferris, A.; Daffos, B.; Urita, K.; Tzedakis, T.; Chauvet, F.; Taberna, P.-L.; Gogotsi, Y.; Simon, P. Capacitive deionization concept based on suspension electrodes without ion exchange membranes. *Electrochem. Commun.* **2014**, *43*, 18−21.

(7) Hatzell, K. B.; Boota, M.; Gogotsi, Y. Materials for suspension (semi-solid) electrodes for energy and water technologies. *Chem. Soc. Rev.* **2015**, *44*, 8664−8687.

(8) Ma, J.; He, C.; He, D.; Zhang, C.; Waite, T. D. Analysis of capacitive and electrodialytic contributions to water desalination by flow-electrode CDI. *Water Res.* **2018**, *144*, 296−303.

(9) Hatzell, K. B.; Eller, J.; Morelly, S. L.; Tang, M. H.; Alvarez, N. J.; Gogotsi, Y. Direct observation of active material interactions in flowable electrodes using X-ray tomography. *Faraday Discuss.* **2017**, *199*, 511−524.

(10) Halfon, E. B.; Suss, M. E. Measurements of the electric conductivity of an electrode as it transitions between static and flowable modes. *Electrochem. Commun.* **2019**, *99*, 61−64.

(11) Gürsoy, D.; De Carlo, F.; Xiao, X.; Jacobsen, C. TomoPy : A Framework for the Analysis of Synchrotron Tomographic Data. *J. Synchrotron Radiat.* **2014**, *21*, 1188−1193.

(12) Chantler, C. Detailed Tabulation of Atomic Form Factors, Photoelectric Absorption and Scattering Cross Section, and Mass Attenuation Coefficients in the Vicinity of Absorption Edges in the Soft X-Ray (Z = 30-36, Z = 60-89, E = 0.1 keV-10 keV), Addressing Convergence I. *J. Phys. Chem. Ref. Data* **2000**, *29*, 597−1048.

(13) Pietsch, P.; Ebner, M.; Marone, F.; Stampanoni, M.; Wood, V. Determining the uncertainty in microstructural parameters extracted from tomographic data. *Sustainable Energy & Fuels* **2018**, *2*, 598−605.

(14) Porada, S.; Bryjak, M.; Van Der Wal, A.; Biesheuvel, P. Effect of electrode thickness variation on operation of capacitive deionization. *Electrochim. Acta* **2012**, *75*, 148−156.

(15) Hatzell, M. C.; Hatzell, K. B. Blue Refrigeration: Capacitive Deionization for Brackish Water Treatment. *Journal of Electrochemical Energy Conversion and Storage* **2018**, *15*, 011009.

(16) Dixit, M. B.; Regala, M.; Shen, F.; Xiao, X.; Hatzell, K. B. Tortuosity Effects in Garnet-Type Li7La3Zr2O12 Solid Electrolytes. *ACS Appl. Mater. Interfaces* **2019**, *11*, 2022−2030.

(17) Bataineh, B.; Omar, K.; Abu-Ain, T.; Abdullah, S. N. H. S.; Abu-Ain, W. Skeletonization Algorithm for Binary Images. *Procedia Technology* **2013**, *11*, 704−709.

(18) Lee, T.-C.; Kashyap, R. L.; Chu, C.-N. Building Skeleton Models via 3-D Medical Surface/Axis Thinning Algorithms. *CVGIP: Graphical Models and Image Processing* **1994**, *56*, 462−478.

(19) Moreno, D.; Hatzell, M. C. Efficiency of Carnot and Conventional Capacitive Deionization Cycles. *J. Phys. Chem. C* **2018**, *122*, 22480−22486.

DOI: 10.1021/acsmaterialslett.9b00106
ACS Materials Lett. 2019, 1, 71−76

(20) Moreno, D.; Hatzell, M. C. Influence of Feed-Electrode Concentration Differences in Flow-Electrode Systems for Capacitive Deionization. *Ind. Eng. Chem. Res.* **2018**, *57*, 8802−8809.
(21) Moreno, D.; Bootwala, Y.; Tsai, W.-Y.; Gao, Q.; Shen, F.; Balke, N.; Hatzell, K. B.; Hatzell, M. C. In Situ Electrochemical Dilatometry of Phosphate Anion Electrosorption. *Environ. Sci. Technol. Lett.* **2018**, *5*, 745−749.

DOI: 10.1021/acsmaterialslett.9b00106
ACS Materials Lett. 2019, 1, 71−76